BIOPHYSICAL CHEMISTRY AND PHYSICAL AND CHEMICAL BIOLOGY

Impact of Drug Repurposing on SARS-Cov-2 Main Protease

Umar Ndagi[a,*]**, Maryam Abdullahi**[b]**, Asmau N. Hamza**[b]**, Mohd G. Magaji**[b]**, Ndumiso N. Mhlongo**[c]**, Makun Babazhitsu**[d]**, Hussaini Majiya**[e]**, Hussaini Anthony Makun**[a]**, and Monsurat M. Lawal**[c]

[a] *Africa Centre of Excellence for Mycotoxin and Food Safety, Federal University of Technology, Minna, Nigeria*
[b] *Faculty of Pharmaceutical Sciences, Ahmadu Bello University, Zaria, Kaduna State, Nigeria*
[c] *Department of Medical Biochemistry, School of Laboratory Medicine and Medical Sciences, University of KwaZulu-Natal, Durban 4001, South Africa*
[d] *Department of Medical Microbiology and Parasitology, Faculty of Basic Clinical Sciences, College of Health Sciences, Usman Danfodio University, Sokoto, Nigeria*
[e] *Department of Microbiology, Ibrahim Badamasi Babangida University, Lapai, Niger State, Nigeria*
* e-mail: ndagiumar2@gmail.com

Abstract—The recent emergence of the severe acute respiratory disease caused by a novel coronavirus remains a concern posing many challenges to public health and the global economy. The resolved crystal structure of the main protease of SARS-CoV-2 or SCV2 (M^{pro}) has led to its identification as an attractive target for designing potent antiviral drugs. Herein, we provide a comparative molecular impact of hydroxychloroquine (HCQ), remdesivir, and β-D-N^4-Hydroxycytidine (NHC) binding on SCV2 M^{pro} using various computational approaches like molecular docking and molecular dynamics (MD) simulation. Data analyses showed that HCQ, remdesivir, and NHC binding to SARS-CoV-2 M^{pro} decrease the protease loop capacity to fluctuate. These binding influences the drugs' optimum orientation in the conformational space of SCV2 M^{pro} and produce noticeable steric effects on the interactive residues. An increased hydrogen bond formation was observed in SCV2 M^{pro}–NHC complex with a decreased receptor residence time during NHC binding. The binding mode of remdesivir to SCV2 M^{pro} differs from other drugs having van der Waals interaction as the force stabilizing protein–remdesivir complex. Electrostatic interaction dominates in the SCV2 M^{pro}–HCQ and SCV2 M^{pro}–NHC. Residue Glu166 was highly involved in the stability of remdesivir and NHC binding at the SCV2 M^{pro} active site, while Asp187 provides stability for HCQ binding.

INTRODUCTION

The recent emergence of an acute respiratory disease caused by a novel coronavirus [1] known as severe acute respiratory syndrome coronavirus 2 (SARS-CoV-2 or SCV2) has become a global threat [2]. This pandemic remains pervasive, posing several challenges to public health and the global economy. World Health Organization (WHO) in February 2020 described the pandemic as coronavirus disease 2019 (covid-19) [3] and characterized with associated high mortality and morbidity [4]. The virus spreads through community transmission in many countries of the world, with European countries badly affected. WHO declared it a public health emergency on January 30th, 2020, and a global pandemic on March 12th, 2020 [4]. With the upsurge in the scientific evidence on coronavirus, there is an increasing understanding of the disease since its emergence [5].

Morphologically, coronaviruses are enveloped single-stranded RNA viruses with about 26–32 kilobases of the genome [6]. They exist in four genera; *Alphacoronavirus* (αCoVs), *Betacoronavirus* (βCoVs), *Gammacoronavirus* (γCoVs), and *Deltacoronavirus* (δCoVs) [6]. The first two families share similar generic attributes and structures with SARS-CoV-2 and infect mainly mammals. The last two genera specifically target birds [7, 8]. The novel SARS-CoV-2 shares the same viral family with the popular Severe Acute Respiratory Syndrome Coronavirus (SARS-CoV) and the Middle East Respiratory Syndrome Coronavirus (MERS-CoV). Also associated with lineage b of Betacoronavirus [9–12], SARS-CoV-2 phylogenetic genome analyses showed a close relationship to SARS-CoV than MERS-CoV [13, 14]. Structurally, the virion is spherical (Fig. 1) with a positive strand of RNA, four structural proteins; spike (S) protein, nucleocapsid (N) protein, membrane (M) protein, envelope (E) protein, and non-structural proteins
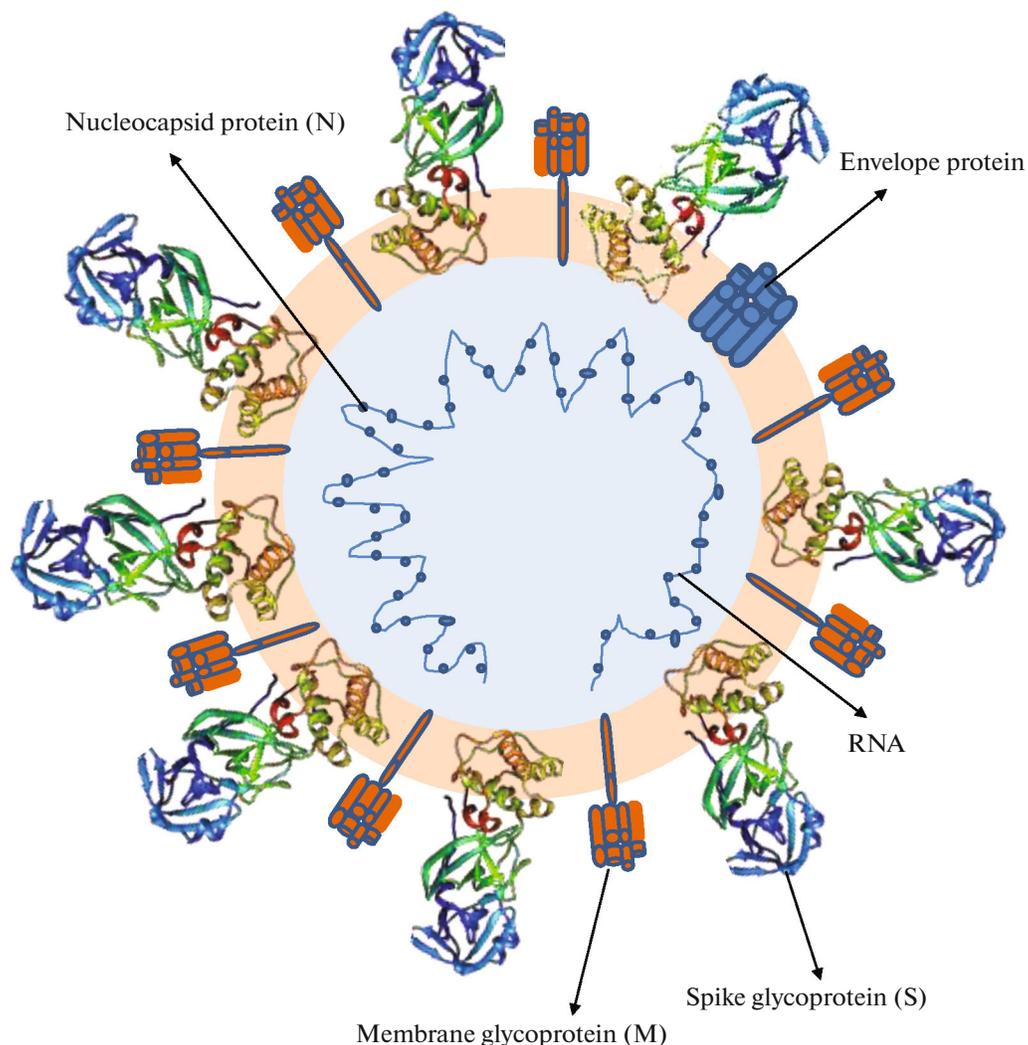
Fig. 1. The morphology of SARS-CoV-2 [25].

(nsp) [15−17]. The viral replication and transcription are driven by the RNA genome enveloped by the N proteins [16]. Like other CoV, the migration of SARS-CoV-2 into the host cells begins with the attachment of S protein on the viral surface to the angiotensin-converting enzyme 2 (ACE-2) of the host cells [18, 19]. Technically, S protein and ACE-2 are considered attractive drug targets [20]. The virus uses host genetic material for replication soon after it penetrates the host cell. Assembling of non-structural proteins (nsp) facilitates the process of viral replication and transcription [16]. These proteins are produced through the cleavage of viral polyprotein encoded by open reading frame 1a (ORF1a) ORF1b [21, 22]. A crucial viral enzyme, RNA-dependent RNA polymerase (RdRp), also known as nsp12, has a vital role in replicating and transcribing the SARS-CoV-2 virus. RdRp catalyzes the synthesis of viral RNA. Therefore, RdRp is also an attractive target for designing antiviral drugs

against covid-19. Also, the nsp7 and nsp8 supports the functions of nsp [23, 24].

Pathogenicity of SARS-CoV-2 revealed the importance of protease in viral structure assembly and replication [26, 27]. In CoVs, ORF1a encodes the main protease (M^{pro}) also known as chymotrypsin-like cysteine protease (3CLPro) [23, 24]. M^{pro} is embedded in the nsp5 region and has a mass of about 33.8 kDa [16], it is encoded by the SARS-CoV-2 RNA sequence [16]. With the protein formation from RNA, M^{pro} is cleaved from the entire protein sequence through an auto-cleavage mechanism [12, 28, 29]. M^{pro} consists of a homodimer divided into two protomers with three different domains (Fig. 2), [30] domains I (residue 8−101), II (residue 102−184), and III (residue 201−303). Between 201−303 residues, five α-helices arranged within a largely antiparallel globular cluster exists, connected to domain II by an extended loop region [2]. These domains identified in the crystal structure
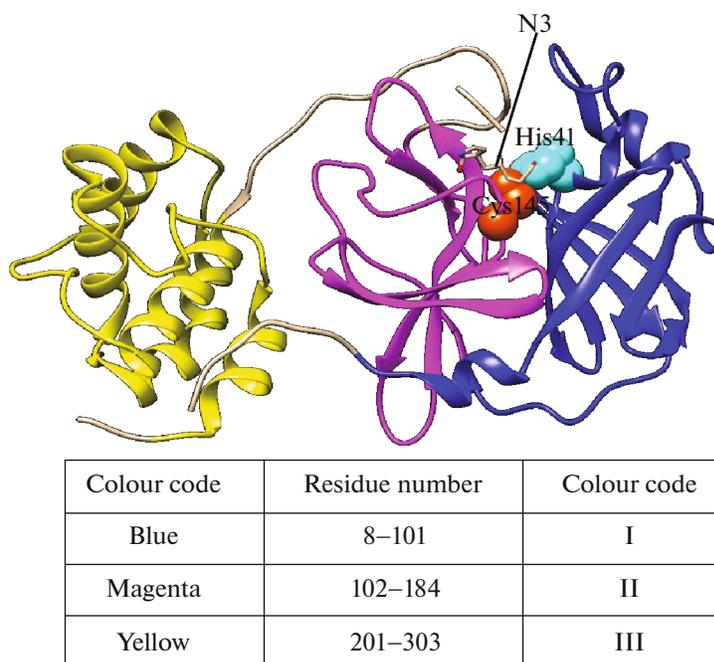
Colour code	Residue number	Colour code
Blue	8−101	I
Magenta	102−184	II
Yellow	201−303	III

Fig. 2. The crystal structure of SARS-CoV-2 M^pro in complex with Michael acceptor inhibitor (N3).

of 6LU7 (the M^pro of SARS-CoV-2) has two catalytic site residues (His41−Cys145) [31−34]. Its substrate-binding site appears in a cleft between domain I and II as the key binding pocket of the SARS-CoV-2 M^pro (Fig. 2). M^pro plays a crucial role in coordinating viral replication and transcription of the virus life cycle. It cleaves the polyproteins' main domain to release proteins with a replicative function such as RdRp and RNA processing domains [35]. Thus, M^pro becomes a principal target for drugs to manage SARS-CoV-2 [36, 37]. Currently, S protein, ACE-2, transmembrane protease serine 2 (TMPRSS2), 3CLpro, RdRp, and PLpro (papain-like protease) are known targets for antiviral drugs against SARS with SARS-CoV-2 [20, 37].

Although the exact cause of SARS-CoV-2 remained a debate, there are indications that viral evolution may be the architect of its emergence [38]. One of the recent studies revealed that ACE-2 facilitates viral migration into the human cell [39]. This process means that SARS-CoV-2 may affect organs with moderate expression of ACE-2 besides the lungs that exist as its prime target site [40]. There are six crucial amino acids in the receptor-binding domain (RBD) of SARS-CoV-like viruses [41, 42]. Thus, the ability of this virus to bind selectively is a result of natural selection [42]. Amino acid residues such as His41, Met49, Gly143, Ser144, Cys145, His163, Met165, Glu166, Leu167, Asp187, Arg188, Ala191, and Glu192 in the structure of SARS-CoV-2 M^pro are described as substrate binding residues [43, 44] and therefore, are essential for drug binding. Details from one research

revealed that the viral S protein (Fig. 1) is the primary determinant of coronavirus tropism [25], this demonstrates the importance of spike proteins in the search for CoV therapeutics.

In a related hypothesis, coronavirus incorporates its spike protein into the viral envelope, thereby facilitating its entry into target cells [45]. The surface unit of the spike protein (S1) binds to the surface receptor. The transmembrane domain (S2) facilitates viral membrane fusion to the cellular membrane [46], these two (S1 and S2) are termed polybasic cleavage sites of SARS-CoV-2 [42]. Cleavage of both S1 and S2 (furin) of the spike protein facilitate the viral entry into human lung cells [46]. Therefore, blockage of these sites can terminate the cascade events and the viral entry process; this might form a promising drug target in SARS-CoV-2 treatment.

Structural insights of the viral morphology by scientists (Fig. 1) led to molecular target identification and possible drugs indicated in the management of SARS-CoV-2. Target identification has opened doors for several computer-aided drug design (CADD) methods, including drug repurposing. Generally, a pandemic demands quick intervention to prevent excessive loss of life. However, the availability of the required medications that will prevent the widespread of the disease and indicated in its treatment would depend on the drug's approval for such disease treatment. Sometimes, drug repurposing is a lucrative option because the drug discovery and approval processes are exhaustive and time-consuming. As a result, a global effort to identify effective treatment was initi-

ated and targeted at agents that demonstrated antiviral activity against SARS-CoV, MERS-CoV, and other related RNA viruses [47]. Though there is no approved antiviral drug for SARS-CoV-2 treatment, preclinical data from hydroxychloroquine (HCQ), remdesivir, and β-D-N^4-hydroxycytidine (NHC) suggested good antiviral activity against SARS-CoV-2. Guided by already existing data from in vitro studies [47], so many drugs, like HCQ, remdesivir, and NHC (Fig. 3), have been repurposed. Accordingly, the best approach to drug discovery during a pandemic is to test whether the existing antiviral drugs are effective in treating related viral infections [48].

Chloroquine (CQ) and hydroxychloroquine (HCQ) are members of a 4-aminoquinoline class used in treating autoimmune diseases. CQ and HCQ have immunomodulatory and antithrombotic properties [49]. They have been frequently used as antimalarial in the last century [49], recommended for treating several viral infections because of their proven potency in the viral cell culture and animal model [49]. The mechanism of action of CQ/HCQ on viral particles has been elusive, the proposed antiviral effect premise on their weak basic properties [49]. Some of the proposed antiviral effects involve *inhibition of viral attachment and entry into the host cell* and *inhibition of new viral particle maturation and spread* [49]. This first process may require (1) inhibition of the sialic acid biosynthesis [50]; (2) inhibition of the N-glycosylation of the cell surface viral receptor ACE-2 [50]; (3) inhibiting the N-glycosylation of the viral S proteins [51]; (4) inhibition of the synthesis of cell membrane sialic acids [51]; and (5) endosomal alkalinization and inhibition of cellular endosomal protease [46]. The second inhibition process requires (1) endosomal alkalinisation and inhibition of endosome-lysosome membrane fusion [52]; (2) endoplasmic reticulum-Golgi intermediate compartment (ERGIC) vesicle alkalinisation and inhibition of viral budding [53]; (3) ERGIC and trans-Golgi network (TGN) vesicle alkalinisation and inhibition of post-translational modification of the

viral protein [10, 54]; (4) inhibition of p38 mitogen-activation protein kinase (MAPK) activation [55, 56]; and (5) inhibition of phospholipase A2 and membranous structures essential for replication and transcription [57].

Recent experimental evidence [49] has demonstrated the potential efficacy of CQ/HCQ in SARS-CoV-2 treatment. A result from an in vitro study reveals an effective blockage of SARS-CoV-2 infection by CQ in Vero E6 cells at a low-micro molar concentration (EC$_{50}$ = 1.13 μM, EC$_{90}$ = 6.90 μM, 48 h), this was clinically achievable within the dose of 500 mg/day oral administration [48]. This same group conducted comparative research on CQ and HCQ effects on SARS-CoV-2 using the same cell model. The result showed relatively similar cytotoxicity between the two drugs [58]. Apart from their anti-inflammatory properties, the potential antithrombotic properties of CQ/HCQ drives its antiviral effect [58]. Several in vitro studies [58−60] conducted to assess the antiviral effects of CQ and HCQ on SARS-CoV-2 revealed significant inhibition of SARS-CoV-2 replication [58−60].

The search for potent antiSARS-CoV-2 against the covid-19 infection led to the scientific basis of exploring the antiviral effect of known drugs. These drugs include remdesivir, favipiravir, ribverin, penciclovir, and galidesivir. Evidence from these studies revealed a better antiviral effect of remdesivir on covid-19 relative to other drug candidates. Remdesivir (GS-5734) is a phosphoramidate prodrug of an adenosine C-nuleoside [61] analogue developed in response to the West Africa 2014 Ebola outbreak [62]. However, the search for potent antiSARS-CoV-2 in the 2019/2020 coronavirus pandemic motivated the exploration of some antiviral drugs. Such drugs include remdesivir, favipiravir, ribverin, penciclovir, and galidesivir. Evidence from these studies revealed a superior antiviral effect on covid-19 relative to other drugs. Remdesivir exhibits broad-spectrum antiviral activity against RNA viruses [62] and inhibits RNA-dependent RNA poly-
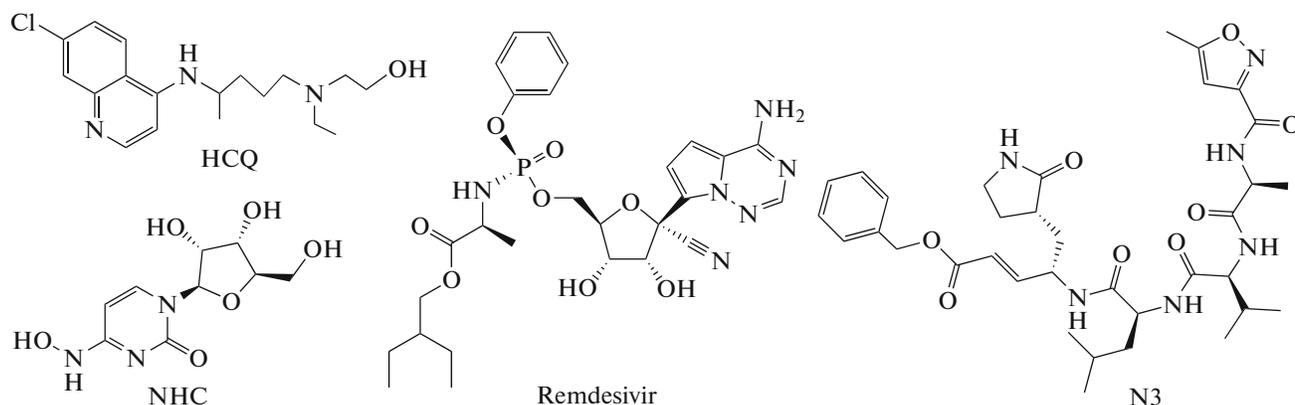

Fig. 3. 2D structures of hydroxychloroquine, remdesivir, β-D-N^4-hydroxycytidine, and N3 used in this study.
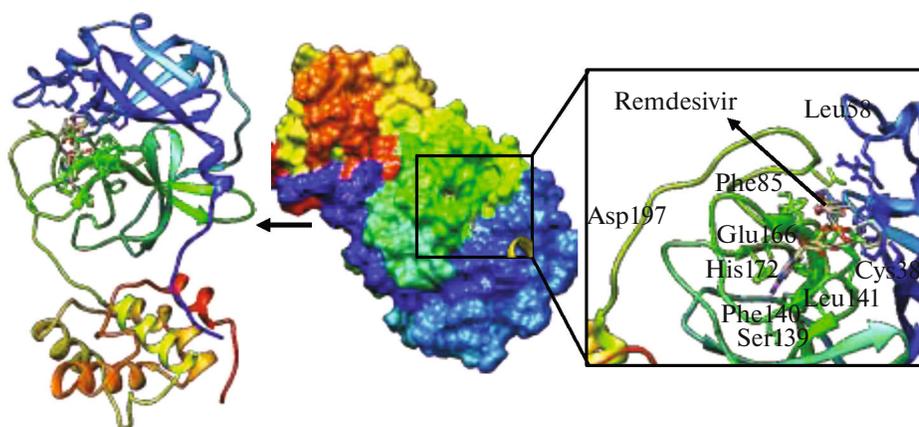
Fig. 4. The crystal structure of SARS-CoV-2 M^{pro} in complex with remdesivir.

merase (RdRp). Gordon et al. [47], showed that incorporating an active triphosphate form of remdesivir into viral RNA by RdRp might lead to the RNA chain termination [47]. They obtained similar observations with SARS-CoV, MERS-CoV, and SARS-CoV-2 RdRps. Based on these pieces of evidence, the researchers concluded that remdesivir triphosphate (RDV-TP) incorporates better than ATP and two other nucleotide analogues [47].

In vitro studies suggest that remdesivir inhibits SARS-CoV and MERS-CoV viruses by interfering with the polymerase function of RdRp [48, 63, 64]. Recent pathogenic events, particularly in European countries, showed that remdesivir administration on patients with severe covid-19 improved their health [65]. This observation made the European Medicines Agency (EMA) approve remdesivir to treat covid-19 patients above 12 yr old [66]. Beigel et al. [67] conducted a double-blind, randomized, placebo-controlled trial of intravenous remdesivir in hospitalized adults with covid-19 and emerging lower respiratory tract infection. Evidence from this study showed that remdesivir was superior to placebo in shortening the time to recovery in hospitalized adults with covid-19 and had evidence of lower respiratory tract infection [67]. Therefore, a molecular understanding of the impact of the interaction between remdesivir and RdRp is required. However, a recent in vitro study [16] suggests that remdesivir binds strongly to RdRp and Mpro—one of the principal targets in designing covid-19 drugs [16]. Based on this research finding [16], comparative dynamics of remdesivir–M^{pro} complex (Fig. 4) and other repurposed drugs could provide relevant information that may form a baseline in designing potent SARS-CoV-2 inhibitors.

NHC is a broad-spectrum ribonucleoside analogue and a potent antiviral drug with marked activity against divergent CoVs [68]. Viral proofreading does not present much effect to its antiviral activity (viral inhibition), giving room for a novel interaction

between nucleoside analogue inhibitor and CoV replicase [68]. Also, the presence of NHC only generate low-level resistance, possibly due to the accumulation of multiple potentially deleterious transition mutation. This phenomenon indicates a mutagenic inhibitory process by NHC and enables the development of NHC in CoVs therapy [68]. NHC demonstrates potent inhibitory activity on MERS-CoV, SARS-CoV, and SARS-CoV-2 in Calu-3 and human airway epithelial (HAE) cells [69]. Surprisingly, NHC inhibited SARS-CoV-2 infection in Vero E6 cells with EC_{50} values of 0.3 and 0.08 μM in Calu-3 cells [69].

After resolving the crystal structure of SARS-CoV-2 M^{pro}, researchers identified M^{pro} as an attractive target for designing potent antiviral drugs [2]. The availability of M^{pro} 3D structure opened opportunities for screening several compounds against it and the discovery of many prospective inhibitors of SARS-CoV-2 M^{pro}, some of which include CQ/HCQ, remdesivir, and NHC. Since there is no antiviral drug approved yet for treating this infection globally (*as of early 2020 when we did this research*), scientists are using evidence of antiviral effects of these drugs to propose them as beneficial in the treatment of covid-19. Although the efficacy and benefit of these drugs to covid-19 infected patients is still unresolved, they are subtly promising with considerable limitations in treating covid-19 [60]. The drugs are related to the side effect and benefit at an appropriate stage of the disease [70]. Owing to the limited evidence on the benefit of CQ/HCQ and other drugs, such as remdesivir and NHC, there is a need for detailed structure to function understanding of SARS-CoV-2 M^{pro}. Such a study would provide information on how potential drug candidates induce changes to known targets of SCV2 M^{pro}.

Here, we show the interaction profile, conformational dynamics, and binding mechanism of SARS-CoV-2 M^{pro} with HCQ, remdesivir, and NHC to give a relative comparison on the molecular effect of these

drugs on SARS-CoV-2 M^{pro}. We used a molecular dynamics (MD) approach over a long simulation period to probe the structural dynamics of this protein when coupled with the selected drugs. The pre-step involves molecular docking of HCQ, remdesivir, and NHC at the active site of SARS-CoV-2 M^{pro}. We used several metrics, including principal component and correlation matrix to probe the structural changes inherent from docking HCQ, remdesivir, and NHC to the protease. The applied computational chemistry approach could enhance drug discovery process [71], providing a platform for novel therapeutics discovery [71].

METHODOLOGY

System Setup and Docking

Researchers have reported a lead compound (Michael acceptor inhibitor, N3) targeting the M^{pro} of SCV2 [2]. N3 is a universal inhibitor of M^{pro} from coronaviruses including SARS-CoV and MERS-CoV2 and exhibited potent antiviral properties against infectious bronchitis virus in the animal model [2, 33]. In this same study, a crystal structure of SARS-CoV-2 M^{pro} in complex with N3 was determined and deposited in the protein data bank (PDB) with code 6LU7 [2]. With the recent determination to proffer a solution to covid-19 through enzyme targeting, the resolved X-ray crystal of SARS-CoV-2 M^{pro} (6LU7, Fig. 4) would facilitate the next generation of clinical therapeutics design against covid-19. SARS-CoV-2 M^{pro} is a prime player in the novel coronavirus infection [62].

We isolated the SARS-CoV-2 M^{pro} enzyme from its co-crystallized N3 and water with Chimera [72], and used the existing chain A for docking. Also, we saved the separated N3 inhibitor in MOL2 while the enzyme was in PDB format with added hydrogen atoms. The optimization of HCQ, remdesivir, and NHC involves applying the steepest descent algorithm and the MMFF94 on the Avogadro GPL V2 [73]. We visualized the resulting molecules with UCSF Chimera 1.13.1 and removed hydrogen atoms from these ligands for subsequent docking.

The molecular docking protocol of the three systems involves docking pose assessment and binding energy prediction using Autodock vina 4.2.6 [74]. We used the Gasteiger partial charges [75] algorithm to assign atomic charges to the ligand and protein from AutoDock via the MGL tools 1.5.6. The grid box dimension (in Å) is $x = 22$, $y = 20$, $z = 20$, and the centre is $x = -19.58$, $y = 18.92$, $z = 64.24$ at 8 exhaustiveness. The box size sufficiently enclosed the HCQ, remdesivir, and NHC structures at the SARS-CoV-2 M^{pro} active site. We performed the docking five times using the Lamarckian algorithm [75] in AutoDock Vina 1.5.6. The docking scores are within -8.7 to -9.8 kcal mol^{-1} for the favored ligand conformations (Table 1).

MD Simulations

The three systems prepared for MD simulations are SCV2 M^{pro}−HCQ, SCV2 M^{pro}−remdesivir, and SCV2 M^{pro}−NHC. Before the MD simulations, we separated the docked protein-ligand complexes and deleted hydrogen atoms from the protein. We assigned protonation to the enzyme via the H^{++} server [76], added hydrogen atoms to the ligands using Chimera software and optimized them in Gaussian 09 [77] at HF/6-31G* level of theory. We used the restrained electrostatic potential (RESP) charge derived on R.E.D server [78] to fit the ligand charges.

We performed the simulations with the Particle Mesh Ewald Molecular Dynamics [79] option in the Amber14 graphics processing machine and the SPFP precision model at two fs timescale. For the ligands, their atomic partial charges was generated using the antechamber formalism via the RESP and GAFF [80]. We set the protein parameters from Amber force field ff14SB [81], and added hydrogen atoms to the protein using the LEaP module implemented in Amber14. The further procedure involves adding counterions and system solvation. The former facilitates neutralization, and the latter improves the protein dynamics. We used an orthorhombic TIP3P water box maintained at a 10 Å distance from the protein surface to the box boundary to maintain continuous and uniform system solvation during the simulation. The long-range electrostatic potential was assigned with the petric-mesh Ewald [79] algorithm at 12 Å nonbonding cut-off. We minimized the energy of the protein-ligand complex in two stages by applying a restrained force at 500 kcal mol^{-1} Å^{-2} on the protein-ligand within 10^3 steps and another unrestraint conjugated gradient minimization at 10^3 steps.

The system was gradually heated in the canonical ensemble (NVT) at 50 ps from 0 to 300 K using the Langevin thermostat [82]. We applied a restraint potential of 5 kcal mol^{-1} Å^{-2} on the protein-ligand at 1 ps collision frequency. An unrestricted equilibration was achieved at 300 K using 2 fs time steps at a constant pressure and temperature for 500 ps using the Berendsen barostat [83] to keep the pressure at 1 atm. The SHAKE [84] algorithm was used to restrict the hydrogen bonds. The production MD runs for 200 ns like the equilibration but at 2 ps pressure-coupling constant. In the MD simulation, we specify coordinates and trajectories saving at every 1 ps of simulation. The analyzed parameters after the MD simulations include root-mean-square deviation (RMSD), root-mean-square fluctuations (RMSF), and radius of gyration (RoG) using the CPPTRAJ [85] program in Amber14. We visualized the trajectories in Chimera software and generated plots using Origin package [86].

Thermodynamics Calculations

Binding free energy is a metric that enables predicting the interaction strength between two or more distinct structures [87–91]. We used the Molecular Mechanics/Generalized-Born Surface Area method (MM/GBSA) [87] to estimate the binding free energy of the selected ligands to the protease. From the MM/GBSA approach, we obtain SCV2 M^{pro}–HCQ, SCV2 M^{pro}–remdesivir, and SCV2 M^{pro}–NHC binding free energy. From the 200 ns trajectory, we took 1000 snapshots for the binding free energy calculation. Following equations show how the MM/GBSA was parameterized to account for the binding free energy:

$$\Delta G_{bind} = G_{protein\text{-}ligand} - G_{protein} - G_{ligand}, \quad (1)$$

$$\Delta G_{bind} = E_{gas} + G_{sol} - T\Delta S, \quad (2)$$

$$E_{gas} = E_{int} + E_{vdW} + E_{ele}, \quad (3)$$

$$G_{sol} = G_{GB} + G_{SA}. \quad (4)$$

In Eq. (2), T and S denote temperature and entropy contribution, respectively. We estimate the S value using the NMODE module of Amber14 [92]. In Eq. (3), E_{gas} denote energy at vacuum, E_{int} represents internal energy, E_{vdW} is van der Waals energy, and E_{ele} denotes Coulomb. In Eq. (4), G_{sol} equals the solvation free energy, which has both polar and non-polar components. We also predicted the individual active site residue energy contribution to the overall free energy.

Principal Component Analysis and Cross-Correlation Matrix

Essential dynamics analysis, popularly known as principal component analysis (PCA), is a metric for measuring protein dynamics [93]. We stripped the solvent molecules and ions from the 200 ns MD trajectories using the CPPTRAJ[85] module in Amber14. The PCA analysis involves C_α atoms of 10^3 frames at 0.1 ns intervals. We calculated the principal components (PC1 and PC2) and the 2 by 2 covariance matrices from the Cartesian coordinates of the protein's C_α atoms. PC1 and PC2 are to the foremost two eigenstates of covariance matrices.

The dynamics cross-correlation matrix (DCCM) allows us to probe time-correlated statistics of the protein residues [94]. To evaluate SCV2 M^{pro}–HCQ, SCV2 M^{pro}–remdesivir, and SCV2 M^{pro}–NHC structural dynamics, DCCMs were generated for the alpha carbon backbone atoms using following equation:

$$C_{ij} = \langle \Delta r_i * \Delta r_j \rangle / \left(\langle \Delta r_i^2 \rangle \langle \Delta r_j^2 \rangle \right)^{1/2}. \quad (5)$$

Note, i and j indicate ith and jth residues, Δr_i and Δr_j is the shift of ith and jth atoms from the average, respectively.

Table 1. Docking energy values and molecular weights of the docked ligands HCQ, remdesivir, and NHC at SARS-CoV-2 M^{pro} active site

Parameter	HCQ	Remdesivir	NHC
Binding energy, kcal mol^{-1}	−8.7	−9.4	−9.8
Molecular weight, g/mol	335.9	602.6	259.2

RESULTS AND DISCUSSION

Docking Analysis and Validation

Compound coupling to a protein structure is a popular molecular modelling approach to determine the most favorable ligand pose within the protein [95]. However, docking may sometimes be unreliable because molecular docking calculation uses static X-ray crystal structures, which lack the essential elements that define a biological environment [90, 91]. So, we performed MD simulations to ensure that the docked complexes remained intact within a specific timescale. Figure 5a shows the SCV2 M^{pro}–HCQ, SCV2 M^{pro}–remdesivir and SCV2 M^{pro}–NHC complexes superimposed on each other. Also, we re-dock N3 and overlay it with the original X-ray structure (Fig. 5b) to validate the quality of the applied docking protocol. The calculated RMSD value between the re-docked and raw PDB structures of N3–M^{pro} is 0.833 Å, denoting less deviation and appreciable accuracy of the docking algorithm.

The docking result showed that NHC has the highest binding affinity of −9.8 kcal mol^{-1} than remdesivir and HCQ with −9.4 and −8.7 kcal mol^{-1}, respectively. The favorable (more negative) interaction energy values of these drug candidates toward SARS-CoV-2 M^{pro} indicate potential inhibition of the protease. This observation corresponds with the experimental result of HCQ, remdesivir, and NHC on covid-19 infected patients [60, 67, 69]. Table 1 shows the docking scores and the molecular weight of each moiety.

System Stability during the MD Simulations

Molecular dynamics simulations of well-relaxed and equilibrated systems conducted at 200 ns for the three systems allowed us to explore the protein complex dynamics. It is imperative to assess ligand-receptor association throughout the MD simulation to achieve the reflected conformational dynamics when sampling trajectories. This evaluation allows measuring the stability of the sampled systems. We measured the system stability and convergence by calculating the alpha carbon atoms RMSD of the proteins over the simulation (Fig. 6).

The RMSD of SCV2 M^{pro}–HCQ, SCV2 M^{pro}–remdesivir, and SARS-CoV-2 M^{pro}–NHC protein structure graphically elucidates the behavior of the systems SCV2 M^{pro}–HCQ system has initial low
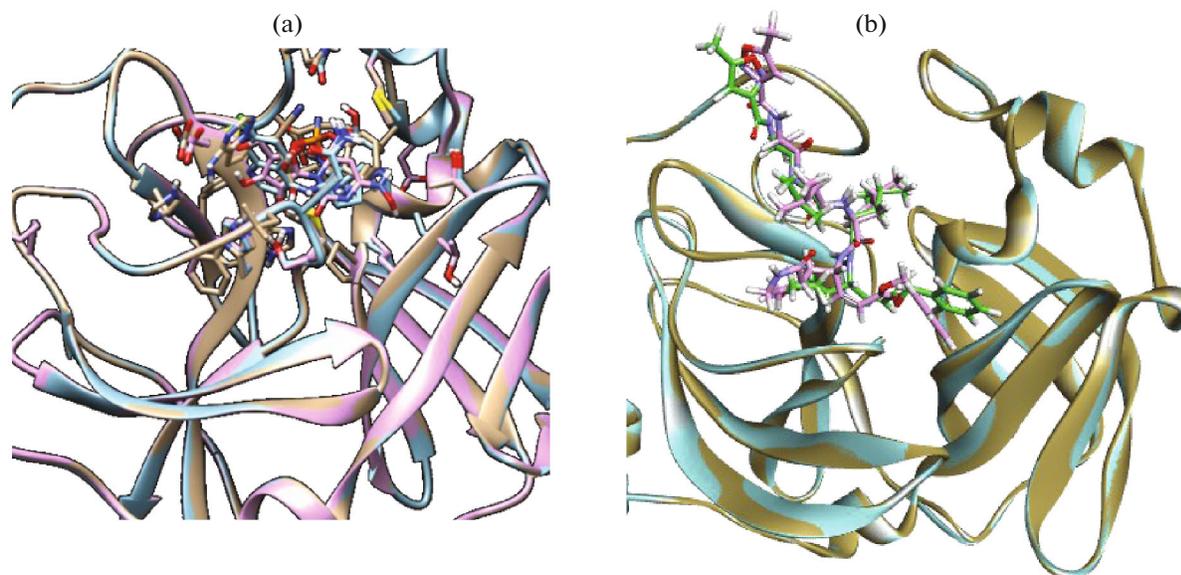
Fig. 5. (a) 3D depiction of the docked SCV2 M^{pro}−remdesivir (light brown), SCV2 M^{pro}−HCQ (cyan), and SCV2 M^{pro}−NHC (pink) superimposed to validate drug binding to the protein active site; (b) re-docked complex of N3−M^{pro}, cyan with ligand (pink) superimposed on the original 6LU7 PDB structure, orange with ligand (green). Image generated with RMSD prediction in the Discovery Studio 2017 R2 [96].
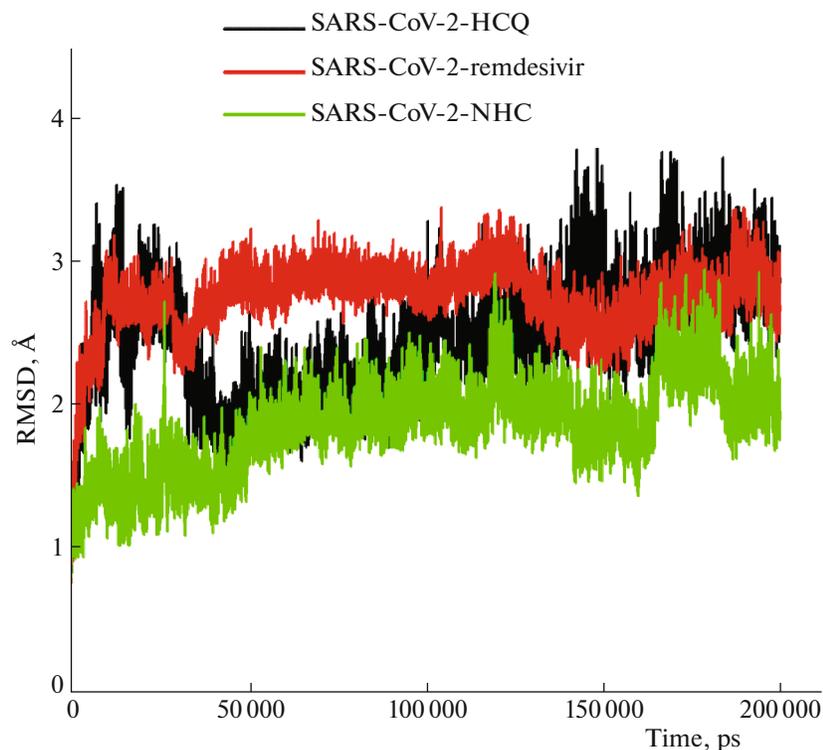
Fig. 6. RMSD of the three systems: SCV2 M^{pro}−HCQ (black), SCV2 M^{pro}−remdesivir (red), and SCV2 M^{pro}−NHC (green).

RMSD fluctuations of 2.3 Å within 0 and 12 500 ps, and later notice an increase in RMSD with the peak RMSD of 3.7 Å at 135 000 ps. After approximately 185 000 ps, the RMSD projections rested below 3.50 Å till the end of the simulation. In SARS-CoV-2 M^{pro}−remdesivir system, the observed highest displacement is 3.3 Å at 100 000 ps, which later rested below 2.8 Å towards the end. Similarly, in SARS-CoV-2 M^{pro}−
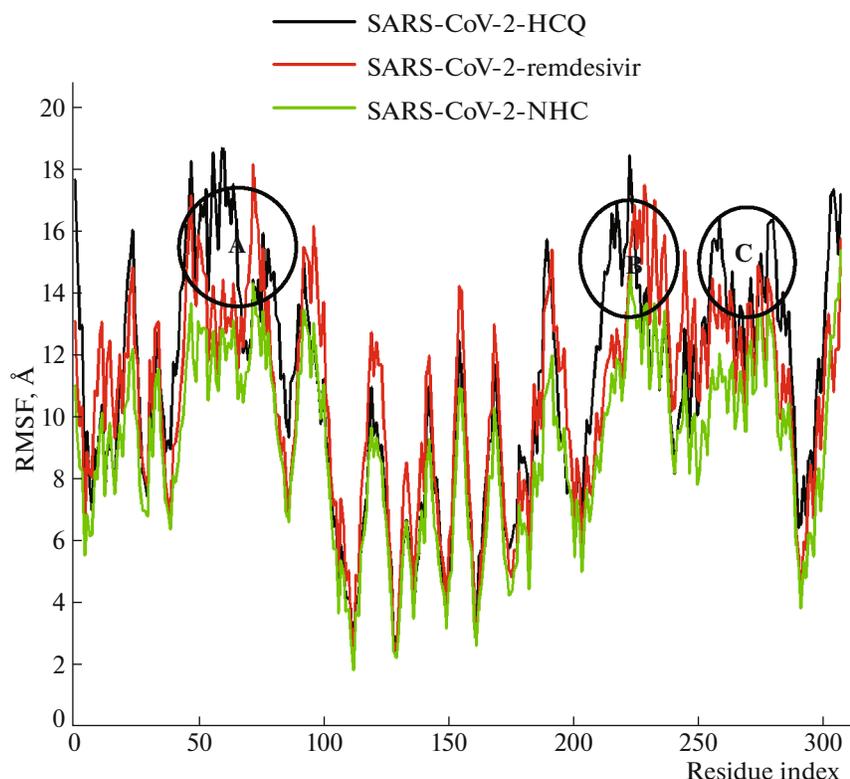
Fig. 7. RMSF plot of atoms within each residue of SCV2 M^{pro}−HCQ (black), SCV2 M^{pro}−remdesivir (red), and SCV2 M^{pro}−NHC (green) systems.

NHC, the peak RMSD of 2.8 Å was reached around 120 000 ps. We recorded the average RMSD of 2.17 and 2.10 Å in SCV2 M^{pro}−HCQ and SCV2 M^{pro}−remdesivir, respectively, while in SCV2 M^{pro}−NHC, the average RMSD is 1.80 Å. These account for the system stability since the standard parameter for a stable system is RMSD of 2 Å and below [88, 97]. RMSD profile in this study is closely related to the RMSD reported recently by Peele et al. [98] and Shivanika et al. [99] for the N3 complex with M^{pro}.

Root Mean Square Fluctuation (RMSF)

The mobility of individual amino acids in proteins defines the overall conformational dynamics of proteins [100, 101]. Consequently, an interaction between the ligand and active site residues may induce conformational changes in the protein structure and alter its function [102]. To explore the dynamic behavior of amino acids of the simulated systems, we calculated the RMSF of the protein residues during the MD simulation. Figure 7 shows the calculated RMSF/Å of each residue atoms when HCQ, remdesivir, and NHC were introduced to SARS-CoV-2 M^{pro} and simulated over the 200 ns. The RMSF profile in this study shows a similar projection to the works from [98, 99].

The protein core (Phe140, Leu141, Asn142, Gly143, Cys145, His163, Met165, Glu166, Leu167, Pro168, Phe185, Asn187, Gln189, Thr190, Ala191, and Gln192), which are catalytic residues [103], looks more compact than the solvent-exposed regions with significant flexibilities. We notice peak fluctuations in loop region **A** involving residue number 25−75 with RMSF values from 16.5 to 18.2 Å in both SCV2 M^{pro}−HCQ and SCV2 M^{pro}−remdesivir. These are catalytic loop residues that perhaps contribute to the ligand binding. However, the RMS fluctuation in SARS-CoV-2 M^{pro}−NHC is minimal relative to the two other systems. In loop region **B**, there is a marginal difference in the loop fluctuations in all the three systems involving residues 200−242, such as Ile200, Leu220, Thr225, Tyr237, and Pro241 with RMSF values from 16.0 to 18.0 Å. The loop region **C** also showcases fluctuations involving residues 250−280 with RMSF values 14.0 to 16.0 Å in SCV2 M^{pro}−HCQ and SCV2 M^{pro}−remdesivir, while SCV2 M^{pro}−NHC show lower fluctuations at this domain.

Note that other loops also exhibit fluctuations but are less prominent than the three regions labelled in Fig. 7. The loop regions (**A**, **B**, and **C**) confer fusion activation and viral cell entry properties [104]. It is evident from the RMSF graph that SCV2 M^{pro}−HCQ exhibits a higher level of fluctuation than the two other
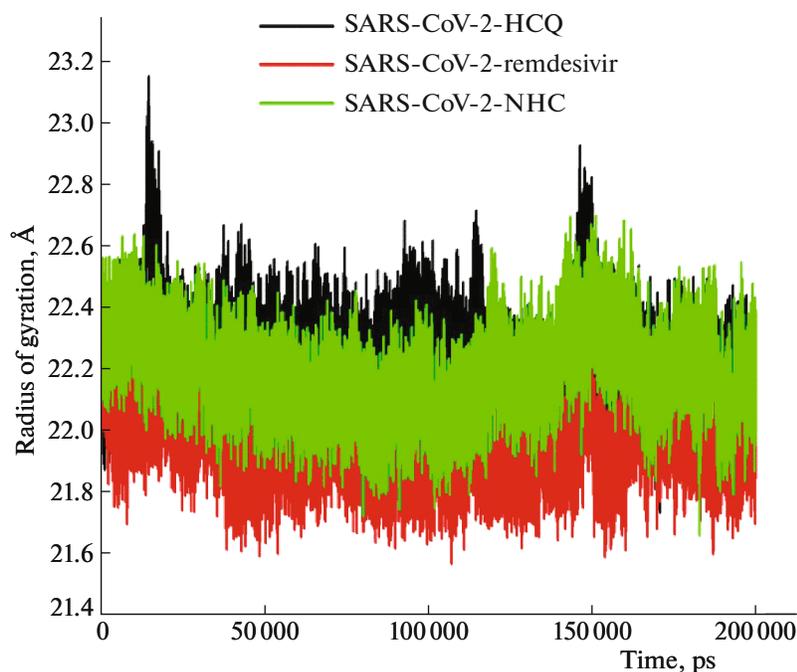
Fig. 8. Projections of all protein atoms radius of gyration when SARS-CoV-2 M^{pro} interact with HCQ (black), remdesivir (red), and NHC (green).

systems. An increase in the fluctuation level reflects the low impact of ligand binding on the protein structure [102]. Therefore, the binding of HCQ on SCV2 M^{pro} has a lower impact on the protein dynamics and may indicate minimal efficacy profile of HCQ in targeting this protease and perhaps in managing covid-19.

NHC binding rigidified the residues and decreased the loop tendency to fluctuate (Fig. 7). This observation conforms with the experimental evidence on the antiviral activity of NHC on other species of coronavirus such as murine hepatitis virus (MHV) and MERS-CoV [68]. The maximum rigidity resulting from the binding process implicates the drug interaction in the active site. This interaction profile follows a decreasing order; SCV2 M^{pro}–NHC, SCV2 M^{pro}–remdesivir, and SCV2 M^{pro}–HCQ. This order is perhaps due to the orientation of these drugs within the protein active site. The maximum rigidity reflects the potency of remdesivir and is likely responsible for faster recovery and fewer interventions that result from using remdesivir in treating covid-19 [62, 67].

The Radius of Gyration (RoG)

RoG is a metric that describes the instantaneous atom inertia from its centre of mass [105]. Radius of gyration is applicable to measure the stability of a biomolecule when perturbed with small compounds over a simulation period. We present the RoG plots of SCV2 M^{pro}–HCQ, SCV2 M^{pro}–remdesivir, and SCV2 M^{pro}–NHC in Fig. 8. There is an associated level of compactness between SCV2 M^{pro}–remdesivir and SCV2 M^{pro}–NHC systems, with the former exhibiting better compactness relative to the latter. However, SCV2 M^{pro}–HCQ shows a lower compactness resulting in a higher mean RoG of 22.57 Å than remdesivir and NHC complexes. The SARS-CoV-2 M^{pro}–remdesivir system has an average RoG of 21.26 Å, while the SCV2 M^{pro}–NHC system has a lower RoG of 21.74 Å. The relatively low compactness exhibited by the SARS-CoV-2 M^{pro}–remdesivir system could indicate remdesivir potential in managing covid-19 as in the Ebola virus [62]. This drug occupies the binding pocket of the protease optimally due to its size (Table 1). Remdesivir exacts favorable firmness to the protein compared to the other two molecules. This observation may be responsible for the clinical efficacy of remdesivir in the treatment of covid-19 and provide a good understanding of the experimental study by Maciorowski et al. [106].

Principal Component Analysis (PCA)

The principal component analysis is also a crucial parameter in molecular modelling, it measures individual atom displacement [107]. We show the PCA plot of the three systems studied herein in Fig. 9. We used the PC clustering approach to measure protein backbone atom displacement. This method can describe different sampled conformations during a simulation by grouping molecular structures into a subset based on their conformational similarities
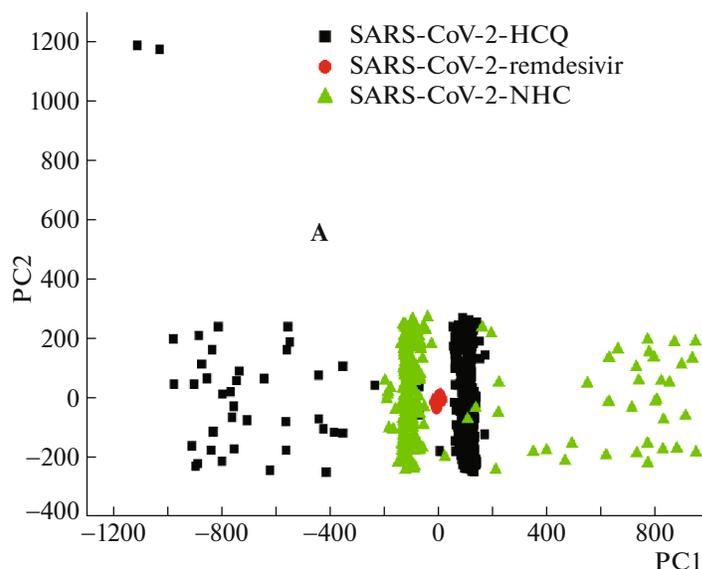
Fig. 9. PCA projection of the alpha carbon displacement created by mapping the first two principal components (PC1 and PC2) in SCV2 M^{pro}–HCQ (black), SCV2 M^{pro}–remdesivir (red), and SCV2 M^{pro}–NHC (green) conformational landscape.

[108]. The eigenvalues used can provide adequate information on the percentage variability or the total mean square displacement of the atom's positional fluctuation captured in each dimension [107]. For proper assessment of protein dynamics and the motions that induce unique molecular attributes, we projected the enzyme towards the first two principal components (PC1 vs. PC2) directions [95]. Figure 9 shows the plots for SCV2 M^{pro}–HCQ and SCV2 M^{pro}–NHC, while SCV2 M^{pro}–remdesivir showed a reasonable association.

Most apparent is the variations in the three complexes observed from their structural features plotted along PC1 and PC2 directions. There is a marked separation of motion in SCV2 M^{pro}–HCQ and SCV2 M^{pro}–NHC, while SCV2 M^{pro}–remdesivir shows more motion correlation with the two principal components PC1 and PC2 (Fig. 9). The SCV2 M^{pro}–HCQ system appears to be more flexible than SCV2 M^{pro}–NHC and SCV2 M^{pro}–remdesivir, suggesting that the binding of remdesivir to the protein (SCV2 M^{pro}) induces a conformational dynamic that reflects in PCs as a wave of motions. In contrast, HCQ and NHC binding to SCV2 M^{pro} impact a few dynamics on the enzyme structure. SCV2–remdesivir system shows a decreased flexibility impacted through remdesivir binding to the protein. This observation corresponds to the experiment of Uzunova et al. [109], whereby remdesivir sufficiently inhibits viral infections in the human cell line. The impact of NHC on the protein structure may be a good description of the mutagenic effect of NHC on the virus main protease [68].

Dynamics Cross-Correlation Matrices (DCCM)

We analyse the DCCM to assess SARS-CoV-2 M^{pro} conformational variations upon ligand binding. DCCM plot analyzed for C$_\alpha$ to examine dynamics and correlated motions is available in Fig. 10. The highly positive correlated and highly negative anti-correlated movement of residues appear in yellow-red and blue-black colors, respectively [95]. The studied systems show more correlated residue motions than anti-correlated. Analysis of the DCCM displays that HCQ binding to SCV2 M^{pro} induces changes to the protein structure.

In SCV2 M^{pro}–HCQ conformation, Arg40 correlates with Leu50, Ala70 correlates with Gly79, while Lys101 slightly correlates with Gln110. Besides, marginally correlated motion exists between Phe150 and Asp155, while a strong correlation is evident between Gln189 and Gly195. Anti-correlated waves of residues in SCV2 M^{pro}–HCQ occur between residues 200 to 306. SCV2 M^{pro}–remdesivir and SCV2 M^{pro}–NHC complexes show correlated and anti-correlated motions, respectively. The SCV2 M^{pro}–remdesivir system exhibit two notable correlated regions; residues 40–130 (strongly correlated regions) and 150–192 (slightly correlated regions). These regions house the catalytic active residues, representing the most intrinsically dynamic portions within the protein. The anti-correlated motions of SARS-CoV-2 M^{pro}–remdesivir appears between residues 210–306. In a related development, the SARS-CoV-2 M^{pro}–NHC system relative to the two other systems exhibits improved correlated motions between residues 20–130 in one region and 150–192 in another domain. Their anti-correlated
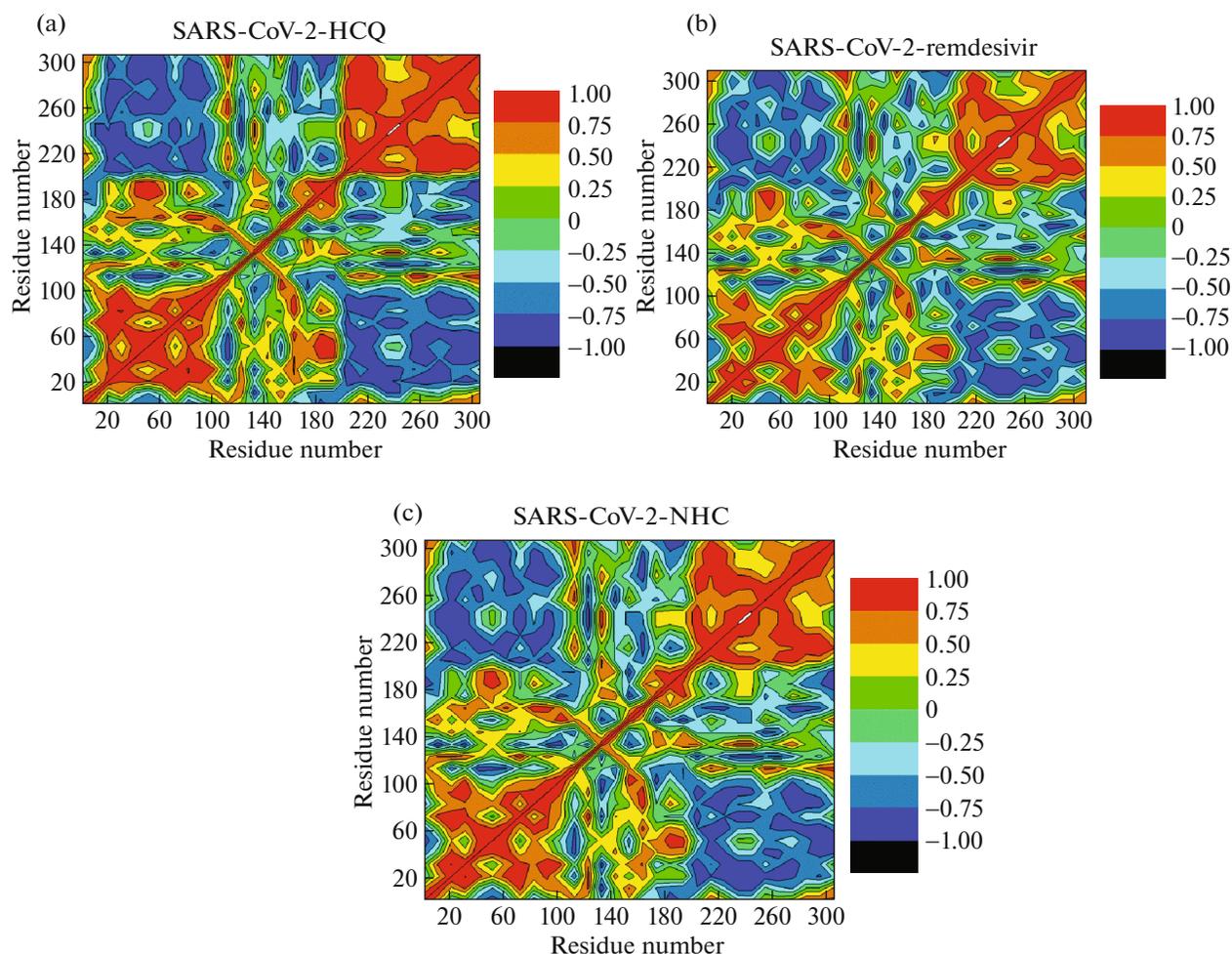
(a)   SARS-CoV-2-HCQ
(b)   SARS-CoV-2-remdesivir

(c)   SARS-CoV-2-NHC

Fig. 10. Cross-correlation matrices of the C_{α} atoms fluctuations in (a) SCV2 M^{pro}–HCQ, (b) SCV2 M^{pro}–remdesivir, and (c) SCV2 M^{pro}–NHC.

waves appear around residues 210–306. The DCCM analysis (Fig. 10) indicates that drug binding to the enzyme significantly impacts the conformational dynamics.

Hydrogen Bonding (H-Bond)

H-Bond formation is crucial to biochemical activities and biological systems, particularly in protein structural integrity maintenance [110]. We assess hydrogen bonds formation over the simulation time, depicted with Fig. 11.

The SCV2 M^{pro}–HCQ shows a lower mean H-bond (140.68) compared to SCV2 M^{pro}–remdesivir and SCV2 M^{pro}–NHC systems with relatively higher mean hydrogen bond of 148.6 and 145.46, respectively. The relative lower H-bond in SCV2 M^{pro}–HCQ could be a response to loop flexibility that invariably affects its binding strength. H-bond reduction might lead to destabilization and dynamics that often impact ligand binding affinity [110]. This explains the possible

reason for better therapeutic outcomes reported from clinical studies [67, 106] on the use of remdesivir compared to HCQ and NHC. To further assess the SCV2 M^{pro}–HCQ, SCV2 M^{pro}–remdesivir, and SCV2 M^{pro}–NHC relative stability, we report their H-bond percent occupancy, average distance, and angle in Table 2.

In the SCV2 M^{pro}–NHC system, the H-bond occupancy for Glu166 is 27% and mean H-bond distance is 2.59 Å. Residue 166 also shows a favored H-bond occupancy of 46% with a mean distance of 2.67 Å in SCV2 M^{pro}–remdesivir complex. Glu166 is a prime active site residue in SCV2 M^{pro}. Val186 exhibits the highest H-bond occupancy (64%) in the SCV2 M^{pro}–NHC system with SCV2 M^{pro}–remdesivir and SCV2 M^{pro}–HCQ systems having Met49 and Leu141 H-bond occupancy contributions of 57 and 89%, respectively. These residues contribute effectively to the ligand-binding having high H-bond occupancy among other active site residues (Table 2).
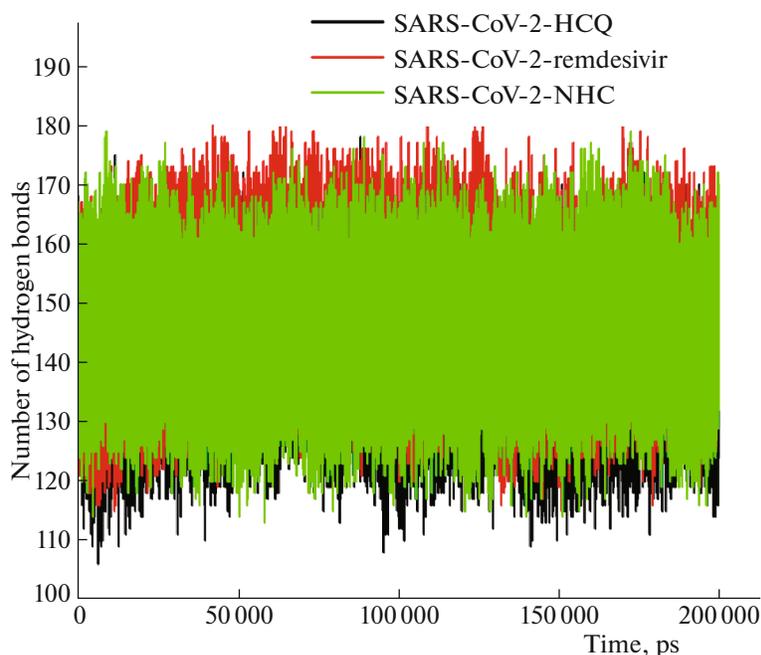
Fig. 11. Hydrogen bonds formed during the simulation run between SCV2 M^{pro}–HCQ (black), SCV2 M^{pro}–remdesivir (red), and SCV2 M^{pro}–NHC (green).

In SCV2 M^{pro}–NHC complex, we recorded a maximum H-bond occupancy of 0.6% between the oxygen atom of the ligand and a nitrogen atom of His41. SCV2 M^{pro}–HCQ and SCV2 M^{pro}–remdesivir display a low H-bond occupancy of 0.01 and 0.05%, respectively, at an average distance of ~2.90 Å linking atoms within the same residue. For the NHC system, the ligand's geometry lies in the conformational space of the M^{pro} at 143°. Remdesivir and HCQ are oriented at angles 145° and 161°, respectively. The angular difference recorded for these ligands in their various conformational space might be responsible for their steric effect. The poses of these ligands in the conformational space of the protein determines its interactive residues, which might determine the mechanism of its viral inhibition [111].

End-Point Free Energy and Its Decomposition

We adopt the MM/GBSA method to calculate the free energy change of SCV2 M^{pro}–HCQ, SCV2 M^{pro}–remdesivir, and SCV2 M^{pro}–NHC complexes (Table 3). Decomposing this energy shows SCV2 M^{pro}–remdesivir with a favored binding energy (-37.2 ± 5.2 kcal mol^{-1}) over SCV2 M^{pro}–HCQ and SCV2 M^{pro}–NHC with calculated values of -36.6 ± 3.3 and -23.5 ± 5.3 kcal mol^{-1}, respectively. The marginal difference between SCV2 M^{pro}–remdesivir and SCV2 M^{pro}–HCQ is -0.60 ± 1.9 kcal mol^{-1}. The energy change in SCV2 M^{pro}–remdesivir and SCV2

M^{pro}–NHC is -13.7 kcal mol^{-1}; this value is quite significant. The most favored interaction energy observed in remdesivir could be the resultant effect of its even occupancy of the protease active region inherent from its size, with a molecular weight of 602.6 g/mol. Note that NHC has a molecular weight of 259.2 g/mol and HCQ with 335.9 g/mol (Table 1).

The force of interaction, such as electrostatic (-46.1 ± 8.8 kcal mol^{-1}) and vdW (-47.7 ± 3.9 kcal mol^{-1}), drive to the overall binding free energy of remdesivir to SCV2 M^{pro} compared to the binding of NHC to the protein. However, SARS-CoV-2 M^{pro}–HCQ exhibits the highest electrostatic (-117.4 ± 10.8 kcal mol^{-1}) and van der Waals forces (-49.6 ± 3.4 kcal mol^{-1}) this may probably contribute to the antiviral properties of HCQ on SCV2 M^{pro}. Hydrophobic packing also contributes to the binding free energy in SCV2 M^{pro}–remdesivir and SCV2 M^{pro}–HCQ systems due to an increased aromatic and hydrophobic rings. Also, there exists some hydrophobic residues in HCQ and remdesivir around the binding pocket, which is relatively low in the SCV2 M^{pro}–NHC system. Interestingly, NHC showed a remarkable binding through the RMSF analysis. Perhaps the low binding energy from MD simulation reflects its molecular weight and indirectly determines NHC receptor resident time [112, 113]. As envisaged, MD provides a more detailed molecular understanding of the complex dynamics relative to molecular docking.

Table 2. Hydrogen bond occupancy at the catalytic region of SARS-CoV-2 bound to HCQ, remdesivir and NHC

H-bond acceptor	H-bond donor	Frame number	Occupancy, %	Average distance, Å	Average angle, deg
SARS-CoV-2–HCQ					
GLN_188@OE1	LIG_307@N3	34719	17	2.82	161
ASP_187@O	LIG_307@O23	21038	10	2.71	161
LIG_307@N17	SER_144@OG	134	0.7	2.86	146
ASP_187@OD1	HIS_41@NE2	164155	82	2.81	159
MET_49@O	TYR_54@OH	87607	43	2.77	162
GLY_143@O	ASN_28@ND2	47846	23	2.86	151
LEU_141@O	SER_144@OG	179624	89	2.74	161
SARS-CoV-2–remdesivir					
GLU_166@O	LIG_307@O6	98088	46	2.67	162
LIG_307@O2	GLN_189@NE2	29952	14	2.84	160
LIG_307@N5	THR_190@N	18230	0.8	2.94	161
SER_144@OG	LIG_307@O5	1642	0.7	2.78	162
LIG_307@N5	GLN_192@NE2	80755	38	2.91	160
ASP_187@O	LIG_307@N6	41143	19	2.84	150
LIG_307@O2	GLN_189@NE2	29952	14	2.84	160
MET_49@O	GLN_189@N	121912	57	2.87	161
LIG_307@O	CYS_44@N	52647	24	2.91	157
GLY_143@O4	HIS_41@NE2	102	0.05	2.90	145
SARS-CoV-2–NHC					
LIG_307@O	HIS_41@NE2	1281	0.6	2.90	143
LIG_307@O1	SER_144@N	1559	0.8	2.88	146
GLU_166@OE2	LIG_307@O6	52992	27	2.6	163
GLN_189@OE1	LIG_307@O2	1598	0.8	2.68	161
LIG_307@O1	SER_144@N	1559	0.8	2.88	146
ASP_187@O	HIS_41@HE2	30376	15	2.85	154
MET_49@O	GLN_189@N	59141	29	2.86	163
GLY_143@O	ASN_28@ND2	17509	8.8	2.87	147
ASP_187@OD2	ARG_40@NH2	127514	63	2.78	160
VAL_186@O	GLN_192@NE2	128980	64	2.86	161

Table 3. MM/GBSA energy (in kcal mol^{-1}) profile of SARS-CoV-2 M^{pro} interaction with HCQ, remdesivir, and NHC

$-\Delta G_{bind}$	$-\Delta E_{ele}$	$-\Delta E_{vdW}$	$-\Delta G_{gas}$	ΔG_{sol}
SARS-CoV-2 M^{pro}–HCQ				
36.6 ± 3.3	117.4 ± 10.9	49.6 ± 3.4	159.0 ± 11.8	122.4 ± 10.6
SARS-CoV-2 M^{pro}–remdesivir				
37.2 ± 5.2	46.1 ± 8.8	47.7 ± 3.9	93.8 ± 10.4	56.6 ± 6.3
SARS-CoV-2 M^{pro}–NHC				
23.5 ± 5.3	36.3 ± 11.4	27.9 ± 3.4	64.2 ± 11.5	40.6 ± 5.3

ΔE_{ele} is electrostatic energy, ΔE_{vdW} is van der Waals energy, ΔG_{bind} is calculated total binding free energy, ΔG_{sol} is solvation free energy.

Table 4. Decomposition of the relative binding free energies (in kcal mol^{-1}) on a per-residue basis for SCV2 M^{pro} binding to drugs HCQ, remdesivir, and NHC

Residues	$-\Delta E_{vdW}$	ΔE_{ele}	ΔG_{polar}	$-\Delta G_{non\text{-}polar}$	$\Delta G_{binding}$
		SARS-CoV-2–HCQ			
His41	1.7 ± 0.4	-2.6 ± 1.6	2.9 ± 1.6	0.1 ± 0.02	-1.4 ± 0.5
Met49	1.2 ± 0.4	-2.1 ± 1.0	1.9 ± 0.9	0.2 ± 0.04	-1.5 ± 0.4
Gly143	0.3 ± 0.1	0.6 ± 0.2	-0.6 ± 0.2	0.03 ± 0.01	-0.3 ± 0.1
Ser144	0.7 ± 0.3	0.1 ± 0.6	0.2 ± 0.4	0.04 ± 0.02	-0.4 ± 0.4
Met165	1.9 ± 0.3	0.9 ± 0.7	-0.8 ± 0.6	0.19 ± 0.04	-1.9 ± 0.5
Glu166	2.9 ± 0.4	-16.9 ± 1.7	19.2 ± 1.9	0.41 ± 0.04	-1.1 ± 0.8
Asp187	0.2 ± 0.7	-25.8 ± 2.3	24.4 ± 1.5	0.08 ± 0.02	-1.2 ± 0.8
Arg188	0.5 ± 0.1	14.4 ± 0.9	-14.1 ± 0.8	0.01 ± 0.01	-0.3 ± 0.3
Ala191	0.01 ± 0.01	0.2 ± 0.1	-0.2 ± 0.1	0.00 ± 0.00	0.01 ± 0.0
Gln192	0.06 ± 0.02	0.97 ± 0.27	-0.91 ± 0.25	0.001 ± 0.004	0.003 ± 0.003
		SARS-CoV-2–remdesivir			
His41	2.2 ± 0.5	-0.4 ± 1.1	1.3 ± 0.8	0.3 ± 0.03	-1.6 ± 0.8
Met49	1.1 ± 0.3	-0.4 ± 0.3	0.6 ± 0.3	0.1 ± 0.04	-1.0 ± 0.3
Gly143	0.6 ± 0.4	-0.8 ± 0.5	1.2 ± 0.7	0.1 ± 0.04	-0.2 ± 0.2
Ser144	0.4 ± 0.6	-2.7 ± 1.6	0.9 ± 0.7	0.1 ± 0.03	-2.3 ± 1.3
Met165	2.1 ± 0.4	-0.6 ± 0.4	0.8 ± 0.3	0.3 ± 0.05	-2.1 ± 0.5
Glu166	1.9 ± 0.7	-10.9 ± 2.1	13.4 ± 1.7	0.5 ± 0.05	0.01 ± 0.8
Asp187	1.1 ± 0.3	-1.6 ± 0.3	2.1 ± 0.4	0.1 ± 0.02	-0.7 ± 0.4
Arg188	0.9 ± 0.2	0.6 ± 0.3	0.1 ± 0.4	0.1 ± 0.02	-0.2 ± 0.3
Ala191	0.04 ± 0.02	-0.05 ± 0.04	0.1 ± 0.05	0.0 ± 0.00	-0.01 ± 0.01
Gln192	0.2 ± 0.1	0.1 ± 0.2	0.2 ± 0.2	0.01 ± 0.01	0.1 ± 0.1
		SARS-CoV-2–NHC			
His41	0.3 ± 0.2	-0.2 ± 0.4	0.4 ± 0.3	0.1 ± 0.03	-0.4 ± 0.4
Met49	0.2 ± 0.4	0.2 ± 0.2	-0.1 ± 0.2	0.1 ± 0.1	-0.2 ± 0.2
Gly143	0.8 ± 0.7	-1.7 ± 0.8	1.4 ± 0.5	0.1 ± 0.03	-1.2 ± 0.5
Ser144	0.9 ± 0.3	-0.9 ± 0.9	0.6 ± 0.5	0.02 ± 0.01	-1.3 ± 0.7
Met165	0.7 ± 0.4	-0.2 ± 0.4	-0.1 ± 0.3	0.04 ± 0.03	-0.6 ± 0.4
Glu166	0.5 ± 0.8	-9.3 ± 3.9	9.4 ± 2.6	0.25 ± 0.03	-0.7 ± 1.5
Asp187	0.1 ± 0.0	-0.9 ± 0.9	0.9 ± 0.9	0.0 ± 0.01	0.01 ± 0.03
Arg188	0.0 ± 0.01	0.8 ± 0.4	-0.7 ± 0.4	0.0 ± 0.0	0.04 ± 0.03
Ala191	0.0 ± 0.0	0.03 ± 0.01	-0.03 ± 0.02	0.0 ± 0.0	0.0 ± 0.0
Gln192	0.01 ± 0.01	0.08 ± 0.07	-0.03 ± 0.1	0.0 ± 0.0	0.03 ± 0.01

All energies are in kcal mol^{-1}, ΔE_{ele} is electrostatic energy, ΔE_{vdW} is van der Waals energy, ΔG_{polar} is polar solvation energy, $\Delta G_{nonpolar}$ is nonpolar solvation energy, $\Delta G_{binding}$ is total binding free energy.
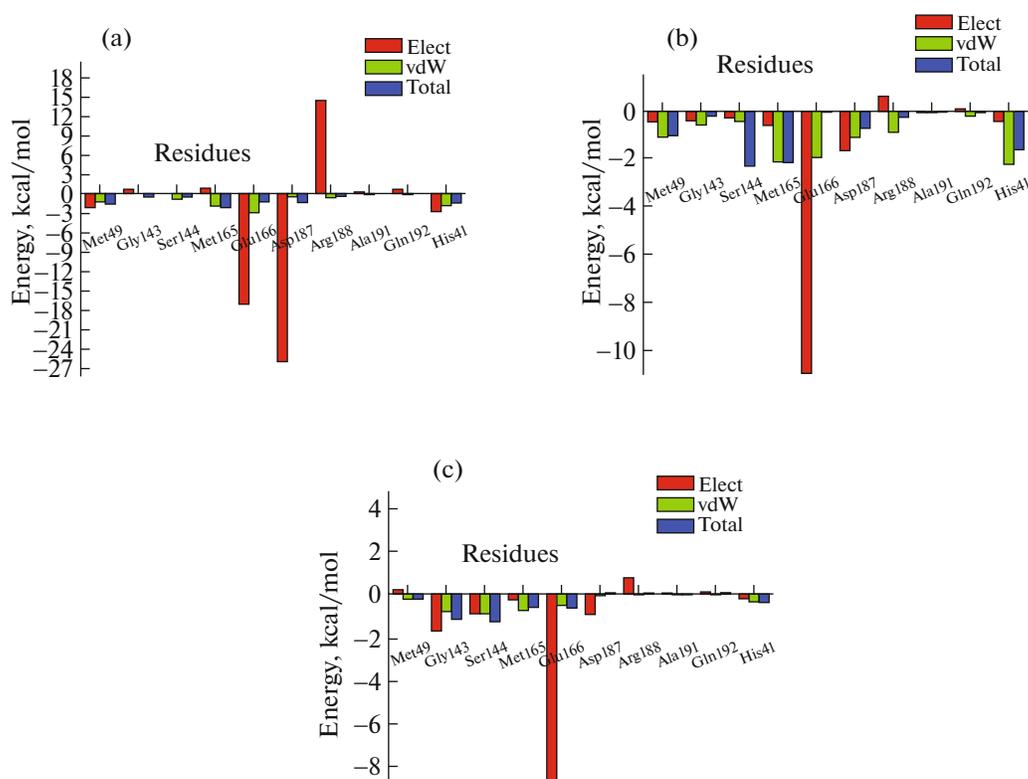
Fig. 12. The per-residue energy decomposition during (a) HCQ, (b) remdesivir, and (c) NHC binding to SCV2 M^{pro}.

Per-Residue Energy Decomposition

The calculated energy decomposition on a per-residue basis is available in Table 4. We show the graphical representation of per-residue energy decomposition analysis of SCV2 M^{pro}–remdesivir, SCV2 M^{pro}–HCQ, and SCV2 M^{pro}–NHC in Fig. 12. In SARS-CoV-2 M^{pro}–remdesivir system, Ser144 contributes to the higher total free energy (-2.1 ± 0.5 kcal mol^{-1}). We observe the same energy contribution pattern in SCV2 M^{pro}–NHC. In this case, Ser144 contributes the highest energy to the ligand-binding site (-1.3 ± 0.7 kcal mol^{-1}), and Asp187 maintained its lowest energy (0.01 ± 0.03 kcal mol^{-1}) contribution to the ligand-binding site. In contrast, Arg188 in the SCV2 M^{pro}–NHC shows the least contribution (0.03 ± 0.02 kcal mol^{-1}) to the total energy compared to other binding residues among the three studied systems.

We observe a generic feature with Glu166 within the systems showing a dominant high electrostatic energy contribution in two of the three systems: SARS-CoV-2 M^{pro}–remdesivir electrostatic contribution -10.9 ± 2.1 kcal mol^{-1} and SARS-CoV-2 M^{pro}–NHC with -9.3 ± 3.9 kcal mol^{-1} (Fig. 12). The emergence of Glu166 in these two systems is a notable development in this study; Glu166 might be a stabilising moiety in remdesivir and NHC binding to SARS-CoV-2 M^{pro}. Asp187 dominates other residues in its

electrostatic contributions (-25.8 ± 2.3 kcal mol^{-1}), representing a stabilising element in HCQ binding to SCV2 M^{pro}. The difference between the stabilising residues might be responsible for the variation in the bioactivity mechanism existing between HCQ and remdesivir/NHC. Although remdesivir and NHC are drugs from different classes, they share the same residue as a bond stabilising factor. This phenomenal stabilising residue indicates a possible novel interaction mechanism with CoV main protease in remdesivir and NHC [114].

Another contributing force to the binding of the ligand to protein is van der Waals. From our result, residues contributing to van der Waal force differ in each system. SARS-CoV-2 M^{pro}–HCQ system gave the highest van der Waal energy (E_{vdW}) contribution from Glu166 (-2.9 ± 0.4 kcal mol^{-1}) and His41 with E_{vdW} of -2.2 ± 0.5 kcal mol^{-1} contribution in SCV2 M^{pro}–remdesivir. SCV2 M^{pro}–NHC system contributes the lowest E_{vdW} of -0.9 ± 0.3 kcal mol^{-1} during the ligand binding (Table 4). It is important to note that E_{vdW}, described as a weak interacting force between the atoms or molecules [115], has a crucial role in ligand-protein binding. For example, the van der Waal contribution of His41 to the binding of remdesivir is fascinating, this residue is one of the catalytic dyads.

In summary, we have employed different computational experiments to unravel the interaction of HCQ, remdesivir, and NHC to SCV2 M^{pro}. The protocols allow a comparative study of the binding mechanism of these drugs to SCV2 M^{pro}. Post-MD analyses, such as PCA, DCCM, hydrogen bonding, thermodynamics calculations, and drug-receptor connectivity network enabled us to study the impact of HCQ, remdesivir, and NHC binding to SCV2 M^{pro}. From the docking analysis, NHC has the favored binding score of −9.8 kcal/mol over remdesivir and HCQ with interacting affinities of −9.4 and −8.7 kcal mol^{-1}, respectively.

The MD study allowed us to estimate the binding conformation of the investigated drugs on SARS-COV-2 M^{pro}. We observed a decrease in the protein loop capacity to fluctuate during the drug binding. We noticed a steric effect of these drugs on the interactive residues. Also, SARS-COV-2 M^{pro}−NHC complex shows appreciable hydrogen bond formation but with the lowest binding free energy reflecting reduced receptor residence time of the drug (NHC). HCQ demonstrated a reasonable level of propensity for SCV2 M^{pro}, plus an increasing number of aromatic and hydrophobic rings in HCQ and remdesivir within the conformational space of the M^{pro} that enhance hydrophobic interaction. We noticed a plausible novel interaction mechanism of remdesivir and NHC with the CoV main protease.

Binding free energy study showed an increase in remdesivir with a value −37.2 ± 5.2 kcal mol^{-1} compared to HCQ and NHC. Remdesivir binds to SCV2 M^{pro} with the most favored total binding free energy, H-bond formation, interaction with the catalytic residues, PCA, DCCM, and RoG. Although NHC showed favorable binding from the docking score and high stability through the RMSD and RMSF plots, it has low electrostatic, van der Waals energy, and binding free energy contributions. This low level of energy contribution with the active site residues in the SCV2 M^{pro}−NHC system might indicate the short receptor resident time of NHC. Hence, this drug candidate may likely be more effective with another antiviral agent, or another covid-19 target.

CONCLUSIONS

Currently, there are other available opinions on the viability of the selected drugs interaction with SCV2 proteins. Despite carrying out this investigation in early 2020, many of the newer experimental claims do not totally negate our observations. For instance, NHC has been noted to be more selective for RNA-dependent RNA polymerase (RdRP) than M^{pro}. Identifying some crucial residue to SCV2 M^{pro} binding in this work aligns with other latest studies. Together with the other identified crucial residues, Glu166 can be engineered towards drug design.

REFERENCES

1. H. M. Mengist, X. Fan, and T. Jin, Signal Transduct. Target Ther. **5** (1), 1 (2020). https://doi.org/10.1038/s41392-020-0178-y

2. Z. Jin, X. Du, Y. Xu, et al., Nature (London, U.K.) **582** (7811), 289 (2020). https://doi.org/10.1038/s41586-020-2223-y

3. WHO Director-General's remarks at the media briefing on 2019-nCoV on February 11th 2020. www.who.int/director-general/speeches/detail/who-director-general-s-remarks-at-the-media-briefing-on-2019-ncov-on-11-february-2020.

4. R. Sharma, M. Agarwal, M. Gupta, et al., in *Coronavirus Disease 2019 COVID-19* (Nature Publ. Group, 2020), p. 55. https://doi.org/10.1007/978-981-15-4814-7_6

5. Coronavirus (COVID-19) Events as They Happen. www.who.int/emergencies/diseases/novel-coronavirus-2019/events-as-they-happen.

6. S. Anastasopoulou and A. Mouzaki, Achaiki Iatriki **39**, 29 (2020).

7. H. Wang, X. Li, T. Li, et al., Eur. J. Clin. Microbiol. Infect. Dis. **39**, 1629 (2020). https://doi.org/10.1007/s10096-020-03899-4

8. J. F. W. Chan, K. H. Kok, Z. Zhu, et al., Emerg. Microbes. Infect. **9**, 221 (2020). https://doi.org/10.1080/22221751.2020.1719902

9. Y. Chen, Y. Guo, Y. Pan, and Z. J. Zhao, Biochem. Biophys. Res. Commun. **525**, 135 (2020). https://doi.org/10.1016/j.bbrc.2020.02.071

10. B. Coutard, C. Valle, X. de Lamballerie, et al., Antiviral Res. **176** (2020). https://doi.org/10.1016/j.antiviral.2020.104742

11. M. Fahmi, Y. Kubota, and M. Ito, Infect. Genet. Evol. **81**, 104272 (2020). https://doi.org/10.1016/j.meegid.2020.104272

12. J. Cui, F. Li, and Z. L. Shi, Nat. Rev. Microbiol. **17**, 181 (2019). https://doi.org/10.1038/s41579-018-0118-9

13. S. F. Ahmed, A. A. Quadeer, and M. R. McKay, Viruses **12** (3), 1 (2020). https://doi.org/10.3390/v12030254

14. M. Pal, G. Berhanu, C. Desalegn, and V. Kandi, Cureus **12** (3), 1 (2020). https://doi.org/10.7759/cureus.7423

15. S. Boopathi, A. B. Poma, and P. Kolandaivel, J. Biomol. Struct. Dyn. **39**, 3409 (2021). https://doi.org/10.1080/07391102.2020.1758788

16. H. L. Nguyen, N. Q. Thai, D. T. Truong, and M. S. Li, J. Phys. B: Chem. **124**, 11337 (2020).
https://doi.org/10.1021/acs.jpcb.0c07312

17. C. Risco, I. M. Antón, L. Enjuanes, and J. L. Carrascosa, J. Virol. **70**, 4773 (1996).
https://doi.org/10.1128/jvi.70.7.4773-4777.1996

18. K. Kuba, Y. Imai, S. Rao, et al., Nat. Med. **11**, 875 (2005).
https://doi.org/10.1038/nm1267

19. H. L. Nguyen, P. D. Lan, N. Q. Thai, et al., J. Phys. B: Chem. **124**, 7336 (2020).
https://doi.org/10.1021/acs.jpcb.0c04511

20. A. Zumla, J. F. W. Chan, E. I. Azhar, et al., Nat. Rev. Drug. Discov. **15**, 327 (2016).
https://doi.org/10.1038/nrd.2015.37

21. L. Enjuanes, *Coronavirus Replication and Reverse Genetics,* Vol. 287 of *Current Topics in Microbiology and Immunology* (Springer, Berlin, 2005).
https://doi.org/10.1007/b138038

22. Y. Chen, Q. Liu, and D. Guo, J. Med. Virol. **92**, 418 (2020).
https://doi.org/10.1002/jmv.25681

23. L. Subissi, C. C. Posthuma, A. Collet, et al., Proc. Natl. Acad. Sci. U. S. A. **111**, E3900 (2014).
https://doi.org/10.1073/pnas.1323705111

24. R. N. Kirchdoerfer and A. B. Ward, Nat. Commun. **10** (1), 1 (2019).
https://doi.org/10.1038/s41467-019-10280-3

25. R. J. G. Hulswit, C. A. M. de Haan, and B. J. Bosch, in *Advances in Virus Research* (Academic, New York, 2016), Vol. 96, p. 29.
https://doi.org/10.1016/bs.aivir.2016.08.004

26. L. Zhang, D. Lin, X. Sun, et al., Science (Washington, DC, U.S.) **368** (6489), 409 (2020).
https://doi.org/10.1126/science.abb3405

27. D. Benvenuto, M. Giovanetti, A. Ciccozzi, et al., J. Med. Virol. **92**, 455 (2020).
https://doi.org/10.1002/jmv.25688

28. S. Kannan, P. Shaik Syed Ali, A. Sheeza, and K. Hemalatha, Eur. Rev. Med. Pharmacol. Sci. **24**, 2006 (2020).
https://doi.org/10.26355/eurrev_202002_20378

29. S. Chen, F. Jonas, C. Shen, and R. Higenfeld, Protein Cell. **1**, 59 (2010).
https://doi.org/10.1007/s13238-010-0011-4

30. Z. Jin, X. Du, Y. Xu, et al., Nature (London, U.K.) **582** (7811), 289 (2020).
https://doi.org/10.1101/2020.02.26.964882

31. K. An, G. J. Palm, J. R. Mesters, et al., J. EMBO **21**, 3213 (2002).
https://doi.org/10.1093/emboj/cdf327

32. H. Yang, M. Yang, Y. Ding, et al., Proc. Natl. Acad. Sci. U. S. A. **100**, 13190 (2003).
https://doi.org/10.1073/pnas.1835675100

33. X. Xue, H. Yu, H. Yang, et al., J. Virol. **82**, 2515 (2008).
https://doi.org/10.1128/jvi.02114-07

34. F. Wang, C. Chen, W. Tan, et al., Sci. Rep. **6** (1), 1 (2016).
https://doi.org/10.1038/srep22677

35. J. Ziebuhr, E. J. Snijder, and A. E. Gorbalenya, J. Gen. Virol. **81**, 853 (2000).
https://doi.org/10.1099/0022-1317-81-4-853

36. V. R. Naik, M. Munikumar, U. Ramakrishna, et al., J. Biomol. Struct. Dyn., 1 (2020).
https://doi.org/10.1080/07391102.2020.1781694

37. C. Liu, Q. Zhou, Y. Li, et al., ACS Cent. Sci. **6**, 315 (2020).
https://doi.org/10.1021/acscentsci.0c00272

38. S. U. Rehman, L. Shafique, A. Ihsan, and Q. Liu, Pathogens **9** (3), 1 (2020).
https://doi.org/10.3390/pathogens9030240

39. P. Zhou, X. Yang Lou, X. G. Wang, et al., Nature (London, U.K.) **579** (7798), 270 (2020).
https://doi.org/10.1038/s41586-020-2012-7

40. M. Y. Li, L. Li, Y. Zhang, and X. S. Wang, Infect. Dis. Poverty **9**, 45 (2020).
https://doi.org/10.1186/s40249-020-00662-x

41. G. Zhou, S. Chen, and Z. Chen, Front Med. **14**, 117 (2020).
https://doi.org/10.1007/s11684-020-0773-x

42. K. G. Andersen, A. Rambaut, W. I. Lipkin, et al., Nat. Med. **26**, 450 (2020).
https://doi.org/10.1038/s41591-020-0820-9

43. T. Muramatsu, C. Takemoto, Y. T. Kim, et al., Proc. Natl. Acad. Sci. U. S. A. **113**, 12997 (2016).
https://doi.org/10.1073/pnas.1601327113

44. M. F. Hsu, C. J. Kuo, K. T. Chang, et al., J. Biol. Chem. **280**, 31257 (2005).
https://doi.org/10.1074/jbc.M502577200

45. M. Hoffmann, H. Kleine-Weber, and S. Pöhlmann, Mol. Cell. **78**, 779e5 (2020).
https://doi.org/10.1016/j.molcel.2020.04.022

46. M. Hoffmann, H. Kleine-Weber, S. Schroeder, et al., Cell **181**, 271e8 (2020).
https://doi.org/10.1016/j.cell.2020.02.052

47. C. J. Gordon, E. P. Tchesnokov, J. Y. Feng, et al., J. Biol. Chem. **295**, 4773 (2020).
https://doi.org/10.1074/jbc.AC120.013056

48. M. Wang, R. Cao, L. Zhang, et al., Cell Res. **30**, 269 (2020).
https://doi.org/10.1038/s41422-020-0282-0

49. E. Quiros Roldan, G. Biasiotto, P. Magro, and I. Zanella, Pharmacol. Res. **158**, 104904 (2020).
https://doi.org/10.1016/j.phrs.2020.104904

50. M. J. Vincent, E. Bergeron, S. Benjannet, et al., J. Virol. **2**, 69 (2005).
https://doi.org/10.1186/1743-422X-2-69

51. J. Fantini, C. di Scala, H. Chahinian, and N. Yahi, Int. J. Antimicrob. Agents **55** (5) (2020).
https://doi.org/10.1016/j.ijantimicag.2020.105960

52. H. Wang, P. Yang, K. Liu, et al., Cell Res. **18**, 290 (2008).
https://doi.org/10.1038/cr.2008.15

53. D. Schoeman and B. C. Fielding, J. Virol. **16** (1) (2019).
https://doi.org/10.1186/s12985-019-1182-0

54. A. R. Fehr and S. Perlman, in *Coronaviruses: Methods and Protocols,* Vol. 1282 of *Methods in Molecular Biology* (Springer, New York, 2015), p. 1.
https://doi.org/10.1007/978-1-4939-2438-7_1

55. M. Kono, K. Tatsumi, A. M. Imai, et al., Antiviral Res. **77**, 150 (2008).
https://doi.org/10.1016/j.antiviral.2007.10.011

56. M. Yang, L. Huang, X. Li, and E. Kuang, Antiviral Res. **133**, 223 (2016).
https://doi.org/10.1016/j.antiviral.2016.08.010

57. J. Thachil, J. Thromb. Haemost. **18** (5), 1 (2020).
https://doi.org/10.1111/jth.14821

58. J. Liu, R. Cao, M. Xu, et al., Cell Discov. **6** (1), 1 (2020).
https://doi.org/10.1038/s41421-020-0156-0

59. A. M. Hashem, B. S. Alghamdi, A. A. Algaissi, et al., Travel Med. Infect. Dis. **35** (2020).
https://doi.org/10.1016/j.tmaid.2020.101735

60. K. Frie and K. Gbinigie, Centre Evid. Based Med. **25**, 1 (2020). www.cebm.net/covid-19/chloroquine-and-hydroxychloroquine-current-evidence-for-their-effec-tiveness-in-treating-covid-19/.

61. D. Siegel, H. C. Hui, E. Doerffler, et al., J. Med. Chem. **60**, 1648 (2017).
https://doi.org/10.1021/acs.jmedchem.6b01594

62. M. A. Hendaus, J. Biomol. Struct. Dyn., **1** (2020).
https://doi.org/10.1080/07391102.2020.1767691

63. M. L. Agostini, E. L. Andres, A. C. Sims, et al., MBio **9** (2), 1 (2018).
https://doi.org/10.1128/mBio.00221-18

64. T. P. Sheahan, A. C. Sims, R. L. Graham, et al., Sci. Transl. Med. **9** (396), 1 (2017).
https://doi.org/10.1126/scitranslmed.aal3653

65. J. Grein, N. Ohmagari, D. Shin, et al., N. Engl. J. Med. **382**, 2327 (2020).
https://doi.org/10.1056/nejmoa2007016

66. Treatments and Vaccines for COVID-19. European Medicines Agency. www.ema.europa.eu/en/human-regulatory/overview/public-health-threats/coronavirus-disease-covid-19/treatments-vaccines-covid-19.

67. J. H. Beigel, K. M. Tomashek, L. E. Dodd, et al., N. Engl. J. Med. **383**, 1813 (2020).
https://doi.org/10.1056/nejmoa2007764

68. M. L. Agostini, A. J. Pruijssers, J. D. Chappell, et al., J. Virol. **93** (24), 1 (2019).
https://doi.org/10.1128/jvi.01348-19

69. G. M. Nitulescu, H. Paunescu, S. A. Moschos, et al., Int. J. Mol. Med. **46**, 467 (2020).
https://doi.org/10.3892/ijmm.2020.4608

70. X. Li, Y. Wang, P. Agostinis, et al., Cell Death Dis. **11** (7), 1 (2020).
https://doi.org/10.1038/s41419-020-2721-8

71. W. Yu and A. D. Mackerell, in *Methods in Molecular Biology* (Humana Press, New York, 2017), Vol. 1520, p. 85.
https://doi.org/10.1007/978-1-4939-6634-9_5

72. E. F. Pettersen, T. D. Goddard, C. C. Huang, et al., J. Comput. Chem. **25**, 1605 (2004).
https://doi.org/10.1002/jcc.20084

73. M. D. Hanwell, D. E. Curtis, D. C. Lonie, et al., J. Cheminform. **4** (8), 17 (2012).
https://doi.org/10.1186/1758-2946-4-17

74. O. Trott and A. J. Olson, J. Comput. Chem. **31** (2), 1 (2009).
https://doi.org/10.1002/jcc.21334

75. R. R. Mittal, L. Harris, R. A. McKinnon, and M. J. Sorich, J. Chem. Inf. Model. **49**, 704 (2009).
https://doi.org/10.1021/ci800390m

76. http://pubs.acs.org/doi/10.1021/jz501780a

77. Gaussian 2009. http://gaussian.com/glossary/g09/.

78. E. Vanquelef, S. Simon, G. Marquant, et al., Nucl. Acids Res. **39**, W511 (2011).
https://doi.org/10.1093/nar/gkr288

79. R. Salomon-Ferrer, A. W. Götz, D. Poole, et al., J. Chem. Theory Comput. **9**, 3878 (2013).
https://doi.org/10.1021/ct400314y

80. J. Wang, R. M. Wolf, J. W. Caldwell, et al., J. Comput. Chem. **25**, 1157 (2004).
https://doi.org/10.1002/jcc.20035

81. J. A. Maier, C. Martinez, K. Kasavajhala, et al., J. Chem. Theory Comput. **11**, 3696 (2015).
https://doi.org/10.1021/acs.jctc.5b00255

82. R. L. Davidchack, R. Handel, and V. M. Tretyakov, J. Chem. Phys. **130**, 234101 (2009).
https://doi.org/10.1063/1.3149788

83. H. J. C. Berendsen, J. P. M. Postma, W. F. van Gun-steren, et al., J. Chem. Phys. **81**, 3684 (1984).
https://doi.org/10.1063/1.448118

84. P. Gonnet, J. Comput. Phys. **220**, 740 (2007).
https://doi.org/10.1016/j.jcp.2006.05.032

85. D. R. Roe, J. Chem. Theory Comput. **9**, 3084 (2013).

86. E. Seifert, J. Chem. Inf. Model. **54**, 1552 (2014).
https://doi.org/10.1021/ci500161d

87. S. Genheden and U. Ryde, Expert Opin. Drug. Dis-cov. **10**, 449 (2015).
https://doi.org/10.1517/17460441.2015.1032936

88. K. Kisten, H. M. Kumalo, K. E. Machaba, et al., Mol. Simul. **47** (16), 1313 (2021).
https://doi.org/10.1080/08927022.2021.1968390

89. A. M. Magwenyane, N. N. Mhlongo, M. M. Lawal, et al., Molecules **25** (8), 1 (2020).
https://doi.org/10.3390/molecules25081785

90. U. Ndagi, N. N. Mhlongo, and M. E. Soliman, Appl. Biochem. Biotechnol. **185**, 655 (2018).

91. U. Ndagi, N. N. Mhlongo, and M. E. Soliman, J. Bio-mol. Struct. Dyn. **36**, 335 (2018).

92. D. A. Pearlman, D. A. Case, J. W. Caldwell, et al., Comput. Phys. Commun. **91** (1), 1 (1995).
https://doi.org/10.1016/0010-4655(95)00041-D

93. U. Ndagi, N. N. Mhlongo, and M. E. Soliman, Mol. BioSyst. **13**, 1157 (2017).
https://doi.org/10.1039/C6MB00848H

94. G. E. Arnold and R. L. Ornstein, J. Biophys. **73**, 1147 (1997).
https://doi.org/10.1016/S0006-3495(97)78147-5

95. U. Ndagi, M. Abdullahi, A. N. Hamza, and M. E. So-liman, RSC Adv. **10**, 145 (2019).
https://doi.org/10.1039/c9ra07204g

96. BIOVIA DS, Discovery Studio Client. www.3ds.com/products-services/biovia/products/mo-lecular-modeling-simulation/biovia-discovery-studio/

97. I. Kufareva and R. Abagyan, Methods Mol. Biol. **857**, 231 (2012).
https://doi.org/10.1007/978-1-61779-588-6_10

98. K. A. Peele, C. Potla Durthi, T. Srihansa, et al., Inform. Med. Unlocked **19**, 100345 (2020).
https://doi.org/10.1016/j.imu.2020.100345

99. C. Shivanika, S. Deepak Kumar, V. Ragunathan, and A. Sumitha, J. Biomol. Struct. Dyn. **40**, 585 (2022).
https://doi.org/10.1080/07391102.2020.1815584

100. M. Tavafoghi Jahromi and M. Cerruti, Cryst. Growth Des. **15**, 1096 (2015).
https://doi.org/10.1021/cg501369q

101. N. Chaffey, B. Alberts, A. Johnson, J. Lewis, et al., Ann. Bot. **91**, 401 (2003).
https://doi.org/10.1093/aob/mcg023

102. E. Ahmad, G. Rabbani, N. Zaidi, et al., J. Biomol. Struct. Dyn. **31**, 630 (2013).
https://doi.org/10.1080/07391102.2012.706081

103. Z. Zehra, M. Luthra, S. M. Siddiqui, et al., Int. J. Biol. Macromol. **161**, 271 (2020).
https://doi.org/10.1016/j.ijbiomac.2020.06.007

104. J. A. Jaimes, N. M. André, J. S. Chappie, et al., J. Mol. Biol. **432**, 3309 (2020).
https://doi.org/10.1016/j.jmb.2020.04.009

105. N. N. Mhlongo, M. Ebrahim, A. A. Skelton, et al., RSC Adv. **5**, 82381 (2015).
https://doi.org/10.1039/c5ra16836h

106. D. Maciorowski, S. Z. E. Idrissi, Y. Gupta, et al., SLAS Discov. **25**, 1108 (2020).
https://doi.org/10.1177/2472555220958385

107. C. C. David and D. J. Jacobs, Methods Mol. Biol. **1084**, 193 (2014).
https://doi.org/10.1007/978-1-62703-658-0_11

108. J. R. Brender and Y. Zhang, PLoS Comput. Biol. **11**, e1004494 (2015).
https://doi.org/10.1371/journal.pcbi.1004494

109. K. Uzunova, E. Filipova, V. Pavlova, and T. Vekov, Biomed. Pharmacother. **131**, 110668 (2020).
https://doi.org/10.1016/j.biopha.2020.110668

110. D. Chen, N. Oezguen, P. Urvil, et al., Sci. Adv. **2**, e1501240 (2016).
https://doi.org/10.1126/sciadv.1501240

111. T. S. Hughes, M. J. Chalmers, S. Novick, et al., Structure **20**, 139 (2012).
https://doi.org/10.1016/j.str.2011.10.018

112. Z. Cournia, B. Allen, and W. Sherman, J. Chem. Inf. Model. **57**, 2911 (2017).
https://doi.org/10.1021/acs.jcim.7b00564

113. S. Wan, A. P. Bhati, S. J. Zasada, and P. V. Coveney, Interface Focus **10**, 20200007 (2020).
https://doi.org/10.1098/rsfs.2020.0007

114. A. J. Pruijssers and M. R. Denison, Curr. Opin. Virol. **35**, 57 (2019).
https://doi.org/10.1016/j.coviro.2019.04.002

115. G. L. Klimchitskaya and V. M. Mostepanenko, arXiv: 1507.02393 (2015).
https://doi.org/10.5862/PROC.516.4